COMMUNICATION

Check for updates

Single stranded 1D-helical Cu coordination polymer for ultra-sensitive ammonia sensing at room temperature†

Taehun Im,[ac] Juyun Lee,[abc] Sung-Chul Kim, [ID] [d] Joharimanitra Randrianandraina,[e] Joo-Won Lee, [ID] [a] Myoung Won Chung, [ID] [f] Taesung Park,[c] Kam-Hung Low, [ID] [g] Seungkyu Lee,[g] Soong Ju Oh, [ID] [c] Yun Chan Kang, [ID] [c] Seunghyun Weon, [ID] [f] Jung-Hoon Lee,[e] Seon Joon Kim [ID] *[abh] and Sohee Jeong [ID] *[a]

With the increasing demand for ammonia applications, there is a significant focus on improving NH_3 detection performance at room temperature. In this study, we introduce a groundbreaking NH_3 gas sensor based on Cu(ı)-based coordination polymers, featuring semiconducting, single stranded 1D-helical nanowires constructed from Cu–Cl and *N*-methylthiourea (MTCP). The MTCP demonstrates an exceptional response to NH_3 gas (>900% at 100 ppm) and superior selectivity at room temperature compared to current materials. The interaction mechanism between NH_3 and the MTCP sensor is elucidated through a combination of empirical results and computational calculations, leveraging a crystal-determined structure. This reveals the formation of NH_3–Cu and NH_3–H_3C complexes, indicative of a thermodynamically favorable reaction. Additionally, Ag-doped MTCP exhibits higher selectivity and a response over two times greater than the original MTCP, establishing it as a prominent NH_3 detection system at room temperature.

New concepts

In this manuscript, we introduce a concept to synthesize and utilize a novel Cu(ı)-based coordination polymer (CP) that exhibits exceptional gas sensing sensitivity and selectivity toward NH_3 at room temperature. On many efforts to develop novel nanomaterials that enable high-performance chemical sensing, polymers, 2D materials, and their hybrids have been studied as an alternative to conventional metal oxide semiconductors, which are limited by low selectivity and high operating temperature. In this manner, CPs have gained attention as they offer tunable electrical properties that can be adjusted through the modulation of metal and ligand components. Here, we highlight the development of a novel sensing material, featuring a unique structure consisting of bundles of semiconducting, single stranded 1D-helical nanowires each with Cu(ı) centers bonded to S atoms in *N*-methylthiourea ligand and Cl atoms (referred to as MTCP). The very narrow electrical conduction pathway in each CP single strand provides an outstanding platform to realize ultrasensitive molecule detection. Remarkably, sensors based on MTCP exhibited up to a 2000% gas response toward 100 ppm NH_3, respectively, which is one of the highest responses ever reported at room temperature among all sensing materials.

[a] *Materials Architecturing Research Center, Korea Institute of Science and Technology, Seoul, 02792, South Korea. E-mail: seonjkim@kist.re.kr, soheejeong@kist.re.kr*

[b] *Convergence Research Center for Solutions to Electromagnetic Interference in Future-mobility, Korea Institute of Science and Technology, Seoul, 02792, Republic of Korea*

[c] *Department of Materials Science and Engineering, Korea University, Seoul, 02841, Republic of Korea*

[d] *Advanced Analysis and Data Center, Korea Institute of Science and Technology, Seoul, 02792, Republic of Korea*

[e] *Computational Science Research Center, Korea Institute of Science and Technology, Seoul, 02792, Republic of Korea*

[f] *School of Health and Environmental Science & Department of Health and Safety Convergence Science, Korea University, Seoul, 02841, Korea*

[g] *Department of Chemistry, The University of Hong Kong, Pokfulam Road, Hong Kong SAR, China*

[h] *Division of Nanoscience and Technology, KIST School, University of Science and Technology, Seoul, 02792, Republic of Korea*

† Electronic supplementary information (ESI) available. See DOI: https://doi.org/10.1039/d4mh00651h

Introduction

Ammonia is a highly versatile gas with a wide range of applications in our daily life and across various industries, including fertilizers and chemicals. In particular, it has emerged as a potential energy carrier for hydrogen storage and transport, holding great promise in the quest for carbon-free fuel. Despite its numerous benefits, ammonia presents significant risks, including health hazards and fire risks, even at ppm-level concentrations. The occupational safety and health administration (OSHA) sets the exposure limit of ammonia to 25 ppm for 8 hours and 35 ppm for 10 minutes.[1] As the use of ammonia continues to rise, it is imperative to develop methods for the sensitive and selective detection of ammonia using gas sensors.

Solid-state-type gas sensors based on semiconductors have been favored and commercialized due to their small size and compatibility with existing electronic devices. To date, metal

oxide semiconductor (MOS) based gas sensors have been extensively employed for ammonia gas detection among various materials due to their high sensitivity and material accessibility. However, MOS gas sensors typically require elevated operating temperatures to enhance their sensitivity, which results in increased power consumption, thermal stress on the sensor, and the need for heating elements.[2,3] Such limitations can be critical in the fabrication of integrative small devices or portable devices which need to operate on low power and in a safer environment. Additionally, MOS sensors exhibit low selectivity toward specific target gases due to the difficulty in engineering molecule-nanoparticle interactions, as gas molecules indirectly interact with the MOS nanoparticles through an oxygen-mediated electron transfer mechanism. As an alternative, gas sensors based on polymers, 2D materials, and composites offer the advantage of operating at room temperature. For instance, polyaniline (PANI) which has some drawbacks like low sensitivity, has showed enhanced NH_3 sensing performance when combined with other functional materials (e.g. carbon materials, MXene, metal oxides).[4–8] However, it is

important that their sensitivity is notably lower compared to MOS sensors.[3,9]

Recently, coordination polymers (CPs) have emerged as a potential solution for room temperature gas sensing.[10,11] CPs represent a hybrid material, combining advantageous properties from both inorganic and organic materials, not only in terms of chemical composition but also overall characteristics. Notably, CPs offer tunable electric properties that can be adjusted by changing the metal centers or ligands, thereby controlling their band gap and conductivity. However, CPs face certain limitations as gas-sensing materials, such as the complexity of synthesis, requiring meticulous control over reactant ratios, reaction conditions, and purification steps, leading to higher production costs. Additionally, most CPs do not exhibit proper electrical conductivity like semiconductors, which hampers efficient signal transduction in response to the target gases.[12] Although a few coordination polymers exhibit a certain level of conductivity, their gas selectivity and sensitivity significantly lack when compared to other materials such as MOS. This deficiency can be attributed to the ineffective overlap
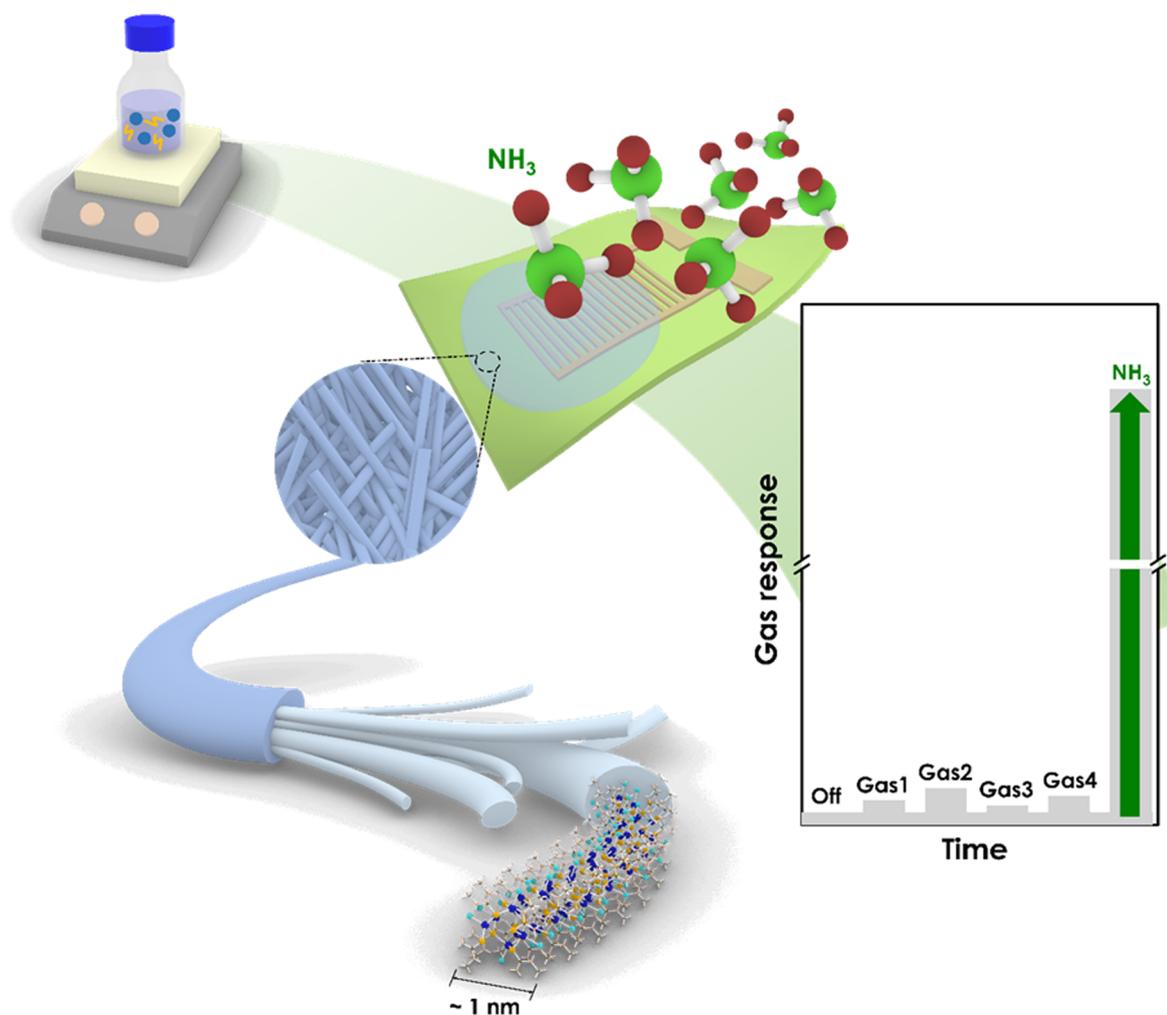
Scheme 1 Schematic illustration of coordination polymer (MTCP) based NH_3 gas sensor. The coordination polymer in the form of nanowires is deposited on the sensing substrate to measure the gas response according to the ambient NH_3 concentration.

between the d orbitals in metals and p orbitals in oxygen- or nitrogen-based redox-interactive ligands bonds, which is commonly found in coordination polymers.[13,14] Furthermore, CPs predominantly form a 3D network, leading to limited charge transport in a single direction. As a result, the formation of electronic conduction network become challenging. To address this limitation, previous studies have suggested using metal–sulfur bonds and 1D network as potential solutions.[15–17] It is believed that these bonds can enhance electronic bonding and charge transport, making coordination polymers more akin to semiconducting or metallic materials like SnO_2 and ZnO. Unlike 3D and 2D pathways, the presence of narrow molecular conduction pathways (*e.g.* 1D network) allows for efficient signal transduction by maximizing changes in electrical resistance upon exposure to the target gas. Among various CPs, coordination polymers incorporating copper metals are a promising for gas sensor material because copper has low toxicity, low cost, and abundance compared to precious and rare-earth metals, and well-established interactions to ammonia molecules. For example, copper sulfide and halide materials were used for ammonia sensing, showing improved selectivity and sensitivity due to the stable interaction between Cu ions and NH_3 molecules through electron transfer from the lone pair electron of N.[18–22] Therefore, copper halide CPs, combined with diverse ligands, as well as copper-organic network CPs utilizing organic-containing ligands, have been employed in gas sensor applications.[23–25]

In this study, we developed an innovative NH_3 gas sensor based on Cu(I) CPs with semiconducting 1D-helical nanowires (referred to as MTCP {[Cu(Cl)(MT)], where MT = *N*-methylthiourea}) (Scheme 1). This MTCP offers several novel features, including Cu–S bonding for semiconductor-like electrical conductivity, a 1D network for efficient signal transduction, and a selective Cu–NH_3 interaction. This sensor exhibits an exceptionally high response to NH_3 gas and superior selectivity at room temperature compared to other existing materials to date. Notably, this coordination polymer can be easily synthesized in ethanol solvents within 10 minutes at room temperature. We have successfully determined the structure of a new coordination polymer consists of a 1D-helical chain constructed with Cu centers bonded to S atoms in MT ligands and Cl atoms, as confirmed by X-ray crystallographic and X-ray spectroscopic analysis. The molecular-level study of the NH_3 reaction mechanism in this MTCP reveals that the effective NH_3 sensing arises from the formation of NH_3–Cu and NH_3–H_3C complexes during exposure of NH_3 gas that is computationally predicted to be highly exothermic. Additionally, Ag-doped MTCP improves both selectivity and reactivity, demonstrating one of the highest reported gas responses toward NH_3.

Results and discussion

Structural analyses of MTCPs

MTCP for NH_3 gas sensing were synthesized using a facile solution-based method at room temperature (RT). Briefly, MTCP

was produced by mixing $CuCl_2$ and *N*-methylthiourea (MT) precursor in ethanol, followed by stirring for 10 minutes at RT. This method is modified from a previously reported synthesis, as described in detail in Methods (ESI†).[26] The MTCP exhibited an average height of 17 nm and an average diameter of 70 nm, as determined by scanning electron microscope (SEM) and atomic force microscopy (AFM) (Fig. 1a and Fig. S1, ESI†). In Fig. 1b, elemental analysis confirms that MTCP is mainly composed of Cu, S, Cl, and N elements, providing further evidence for its nanosized, one-dimensional structure. The MTCP material was synthesized as bundles of multi-domain twinned crystals (Fig. S2, ESI†), and despite the challenges posed by these crystal samples, we were able to determine the atom connectivity and molecular geometry of the polymeric structure through single-crystal X-ray diffraction (SCXRD) analysis. The obtained low-temperature SCXRD structure model served as the initial model for refining the room-temperature powder X-ray diffraction (PXRD) pattern of the bulk material. The observed differences between the low-temperature SCXRD structure and the room-temperature PXRD structure in unit cell parameters and space group can be attributed to the effect of a significant degree of thermal motion of atoms at higher temperatures. The PXRD pattern was indexed to reveal that the MTCP material adopts the $P4_1$ tetragonal space group with lattice parameters a = 11.311(3) Å and c = 7.1710(1) Å. Additional crystallographic details can be found in Table S1 (ESI†). In Fig. 1c, the infinite rod-like structure of MTCP is displayed. The Cu^+ metal center is bonded to one Cl^- anion and three S atoms of the MT ligand, while each S atom of the MT ligand is bonded to three CuCl units. The alternative coordination of metal chloride and MT ligands resulted in the formation
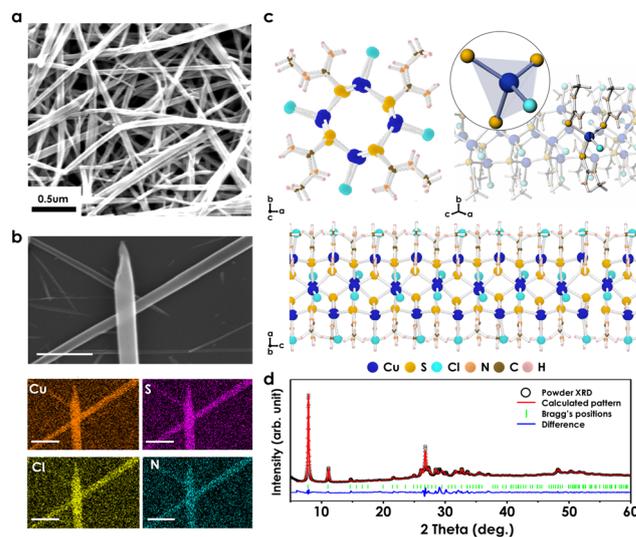

Fig. 1 Structure analyses of MTCP. (a) SEM image showing the overall morphology and (b) EDS mapping result of MTCP (scale bar: 0.5 μm). (c) MTCP structure and coordination environment of Cu(I) in MTCP obtained from single crystal XRD and computing simulation. Blue, yellow, aqua, orange, brown, and pink spheres indicate copper, sulfur, chlorine, nitrogen, carbon, and hydrogen, respectively. (d) Pawley refinement of PXRD pattern for MTCP powder with the starting model obtained from SCXRD analysis.

of boat-shaped Cu_3S_3 six-membered rings in the periphery and distorted crown-shaped Cu_4S_4 eight-membered rings in the core. These fused rings form a 1D chain through contiguous Cu centers linked *via* MT ligands, exhibiting screw symmetry in the *c*-axis direction to create a 1D-helical structure (Fig. S3, ESI†). Each chain exists as individual, single strands where the synthesized MTCP contains multiple strands physically bound together. Importantly, the crystal structure of the polycrystalline MTCP sample was determined through PXRD analysis using the Pawley method.[27] The R_{wp} value obtained was 2.89%, as calculated using the TOPAS program,[28] as depicted in Fig. 1d.

To elucidate the structural characteristics of MTCP, we conducted a comprehensive analysis of its composition and bonding states using Fourier transform infrared spectroscopy (FTIR), X-ray photoelectron spectroscopy (XPS), and X-ray absorption spectroscopy (XAS). In Fig. S4 (ESI†), upon comparing the FTIR peaks of MTCP with those of the MT precursor, significant shifts were observed in the peaks corresponding to N–H stretching vibrations from 3254 cm^{-1} to 3290 cm^{-1}. This shift can be attributed to the highly polar structure resulting from the formation of Cu–S bonds.[29,30] Furthermore, the intensity of strong peaks within the range of 1100 to 900 cm^{-1}, corresponding to C=S vibrations, decreases due to the generation of Cu–S bonds.[29–31] The generation of these bonds also causes shift in certain peaks related to N–H vibrational properties from 1296 cm^{-1}, 1404 cm^{-1}, and 1556 cm^{-1} to 1302 cm^{-1}, 1420 cm^{-1}, and 1585 cm^{-1}.

Bonding and electrical characteristic of MTCPs

In the XPS spectra, the Cu 2p spectrum exhibits prominent peaks at 931.4 eV and 951.3 eV, clearly showing the Cu^+ oxidation state within MTCP.[32] Furthermore, the S 2p spectrum of MTCPs is distinct from that of the pure ligand (Fig. 2a shown in gray) where the peaks in MTCP shifted to higher binding energies of 161.7 eV and 163 eV, primarily attributed to the Cu–S bonds. These binding energies are similar to those reported for Cu(I)–S bonds in previous literature.[33,34] In the Cl 2p spectrum, the two distinct peaks at 196.8 eV and 198.4 eV indicate the existence of copper–chlorine bonds.[35] Additional spectra at the C 1s and N 1s core regions also clearly showed the main chemical bonds that exist in MTCP, as shown in Fig. S5 (ESI†).

In order to better understand of the coordination of Cu and ligand in MTCP, we also performed Cu K-edge and L-edge XAS analyses (Fig. 2b and c). For 3d metals, K-edge XAS primarily probes $1s \rightarrow 4p$ transition, while $L_{3,2}$-edge XAS probes $2p \rightarrow 3d$ transition. The white-line absorption of Cu K-edge of MTCP, primary indicator of the Cu oxidation, resembles that of CuCl rather than $CuCl_2$. This alignment suggests that the oxidation state of Cu in MTCP is +1, which is also supported by the result obtained by XPS analyses. Furthermore, L-edge spectra, including both surface-sensitive total electron yield (TEY) and bulk-sensitive total fluorescence yield (TFY) spectra, was investigated to observe the details of ligand coordination (Fig. 2c). For copper chlorides, the peak at 930.8 eV was detected in both TEY and TFY spectra, indicating the oxidation of the Cu species and showing a local structure consistent with CuO.[36,37] On the other hand, the TEY and TFY spectra of MTCP show a very weak signal in this region in the both the surface and bulk of MTCP, suggesting that the Cu(I) in MTCP maintains a robust coordination with the ligands with good oxidation resistance. It is important to note that Cu(I) is known to be well oxidized and can easily be formed CuO.[38,39]

Moreover, the Cu L-edge X-ray absorption near edge structure (XANES) spectra shows distinctive hybrid state in MTCP compared to copper chlorides. In the TEY and TFY spectra of MTCP, a new peak was observed at 936 eV which is higher energy than the 933.5 eV typically associated with Cu(I) compound.[37] Previous reports have established that the interaction between a metal with filled d-orbitals and ligands, facilitated by π back-bonding contribution, leads to the appearance of a high-energy peak in L-edge spectra.[40,41] Interestingly, this spectral feature is also observed in MTCP, which suggests the strong interaction between the central Cu(I) atom and the thione ligand, as confirmed by IR and X-ray spectroscopic analyses as well.[42] Additionally, the peak at 936 eV exhibits a comparable intensity to the lower energy feature at 933.5 eV, which suggests electron transitions into an antibonding orbital with a significant Cu-d character, associated with thione π back-bonding interaction.[43,44] In overall, these spectroscopic distinctions of MTCP from other copper–chlorine compounds, such as CuCl or $CuCl_2$, signifies the formation of a new bond between Cu–Cl and MT ligand.

To further comprehend the electrical properties of MTCP, electrical conductivity measurements were conducted using a 2-point probe current measurement technique (Fig. S6, ESI†). The conductivity and resistivity of MTCP were calculated by employing Ohm's law, wherein the dimensions of sample and the measured current were considered as variables. As a results of these calculations, it was determined that MTCP exhibits a temperature coefficient of resistivity (TCR) of -0.020 K^{-1}. Notably, the negative TCR aligns with the characteristic behavior commonly associated with semiconductors, suggesting that MTCP possess semiconducting properties. To further elucidate
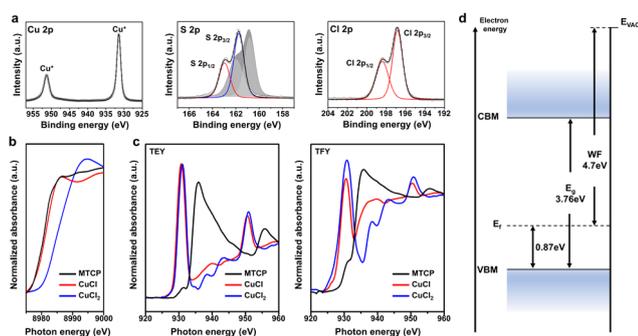

Fig. 2 (a) XPS spectra at the Cu 2p, S 2p, and Cl 2p core regions for MTCP. The gray background in the S 2p spectrum represents data of the *N*-methylthiourea precursor while solid line represents MTCP data. (b) and (c) XAS analysis for MTCP. (b) Cu K-edge and (c) L-edge XANES spectra of MTCP compared to standard Cu–Cl compounds. (d) Electronic band diagram of MTCP determined *via* UV-vis and UPS.

the band diagram of the semiconducting MTCP, ultraviolet-visible spectroscopy (UV-vis) (Fig. S7a, ESI†) and ultraviolet photoelectron spectroscopy (UPS) (Fig. S8, ESI†) were carried out. The Tauc plot in Fig. S7b (ESI†) revealed that the bandgap of MTCP was 3.76 eV, which is similar to those of semiconducting metal oxides commonly used in gas sensors, such as SnO_2 (3.6 eV).[45] UPS measurements revealed that the work function (WF) of MTCP was 4.7 eV, while the valence band maximum (VBM) was 0.87 eV below from the Fermi level. Combining these results, a band diagram for MTCP could be drawn as shown in Fig. 2d. The band diagram clearly shows that MTCP would be a p-type semiconductor as the Fermi level is closer to the VBM than the conduction band minimum (CBM).

Gas sensing properties of MTCP sensor

In order to evaluate the gas sensing performance of MTCP, sensors were prepared by drop-casting MTCP dispersed in ethanol onto gas sensing electrodes to form a film (Note S1 and Fig. S9, ESI†). Here, MTCP was the only material included in the drop solution used to manufacture gas sensors, except for ethanol used as the solvent. Then, sensors were exposed to various concentrations of NH_3 gas in a sealed chamber while the electrical resistance was dynamically measured in a two-electrode chemiresistor setup. Here, the gas response was measured by the relative change in electrical resistance (gas response = $(R - R_0)/R_0 \times 100\%$, R = dynamic resistance, R_0 = baseline resistance). Importantly, all tests were performed at room temperature. Fig. 3a shows the I–V curve of MTCP sensor, measured within the operating voltage range and the observed linear correlation in the entire range indicates well-established contacts between the electrodes. Additionally, real-time gas response measurements of MTCP were conducted under 0.25–100 ppm NH_3 conditions (Fig. 3b and c) where the graphs based on actual resistance values is in Fig. S10 (ESI†). It can be seen that MTCP shows a very high gas response at room temperature, with a response of 915% for 100 ppm NH_3. Here, the MTCP sensor exhibited a response time of 403 s and a

recovery time of 711 s toward 100 ppm NH_3 at room temperature. Notably, MTCP also showed a significant gas response at lower NH_3 concentrations of 0.25–5 ppm (Fig. 3b) with a gas response of approximately 5% at 250 ppb NH_3. With a signal-to-noise ratio (SNR) of response at 0.25 ppm is 10, this suggests the capability of MTCP to detect even lower NH_3 concentrations, although not tested in this study. Fig. 3d compares the maximal gas response of MTCP toward 0.25–100 ppm NH_3, showing a linear correlation between gas concentration and response within the wide concentration range. Also, importantly, MTCP sensors exhibited reliable gas responses when repeatedly exposed to 100 ppm NH_3 for multiple cycles (Fig. 3e). Furthermore, the gas sensing performance of MTCP toward NH_3 was also measured under an air environment (Fig. S11, ESI†). The overall response curve and gas response was similar to what was observed under a N_2 environment.

Sensing mechanism

To understand the adsorption mechanism of NH_3 on MTCP, we performed *in situ* diffuse reflectance infrared Fourier transform spectroscopy (DRIFTs) measurements combined with first-principles density-functional theory (DFT) calculations. For the *in situ* DRIFTs measurements, samples were placed in a sealed cell and subsequently exposed to 300 ppm NH_3 gas (Fig. 4a). In order to mitigate the potential interference of signals originating from the amine functional groups of MTCPs, the initial spectrum of MTCP was used as the baseline. The broad peak in the range between 3400 cm^{-1} and 2900 cm^{-1} can be attributed to the N–H stretching and vibration mode of NH_3.[46] Notably, the intensity of this peak increased with prolonged exposure time, suggesting an evolving interaction. The peaks at 1661, 1460, and 1415 cm^{-1} represent the interaction between NH_3 and the Brønsted acid site within the
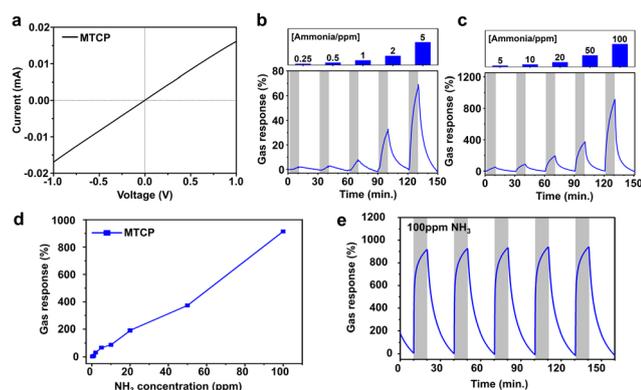

Fig. 3 (a) I–V curve of MTCP sensors coated on sensing electrodes. (b) and (c) Dynamic gas response of MTCP towards (b) 0.25–5 ppm NH_3, (c) and 5–100 ppm NH_3. (d) Correlation between gas response of MTCP and NH_3 concentration. (e) Dynamic gas response of MTCP toward repeated injections of 100 ppm NH_3.
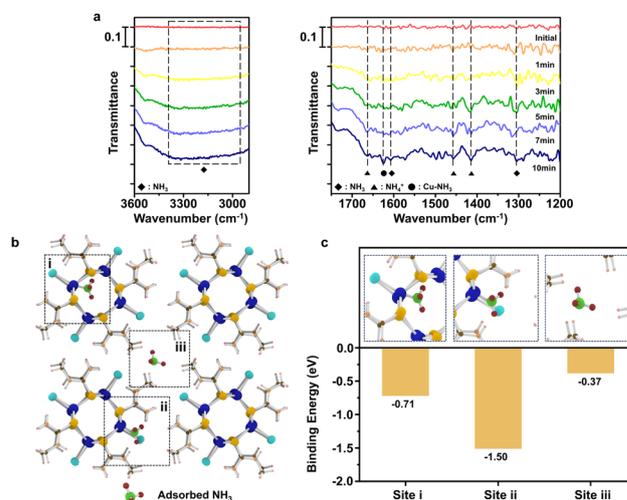

Fig. 4 (a) *In situ* DRIFTs spectra of MTCP in the initial state and those after exposure to 300 ppm NH_3 for 1, 3, 5, 7, 10 min. (b) Predicted NH_3 adsorption sites in MTCP by DFT calculations. i. Interaction with Cu from the inner side of the Cu–S channel ii. Interaction with Cu from the outer side of the Cu–S channel iii. Interaction with four CH_3 groups. (c) Calculated binding energies at each adsorption site.

MTCP (NH$_3$···H),[46,47] while the peaks at 1608, and 1305 cm^{-1} represent the interaction between NH$_3$ and Lewis acid site (Cu$^+$).[48] Interestingly, an additional peak corresponding to NH$_3$–Cu(I) binding at 1627 cm^{-1} was also identified.[46,49] Taken together, these observations suggest that NH$_3$ molecules closely interact with both the hydrogen atoms of ligands and Cu(I) atoms.

Using DFT calculations, we elucidated energetically favorable NH$_3$ binding sites in MTCP to further understand the adsorption mechanism at the molecular level. As spectroscopy analyses revealed the chemical binding of NH$_3$ with Cu, this case was initially investigated. DFT calculations revealed that there are two favorable binding sites for this case: (i) NH$_3$ binding to Cu within the Cu–S channel (panel (i) of Fig. 4b), leading to a N (in NH$_3$)–Cu distance of 2.08 Å with a binding energy of −0.71 eV, and (ii) NH$_3$ binding to Cu from outside of the Cu–S channel (panel (ii) of Fig. 4b) where NH$_3$ replaces with Cl atoms with a stronger binding energy of −1.50 eV at a N (in NH$_3$)–Cu distance of 2.01 Å. Such binding behaviors are consistent with a previous study on Cu(I)–halide compounds for NH$_3$-selective gas sensors, showing that Cu ions and NH$_3$ are likely to form ammine complexes.[20]

Moreover, another stable NH$_3$ binding site was revealed using *ab initio* molecular dynamics (AIMD) calculations (see panel (iii) of Fig. 4b and Fig. S12, ESI†). As shown in Fig. S12 (ESI†), NH$_3$ initially interacts with amine units in MTCP at a calculated binding energy of −0.25 eV, which then moves in between two methyl groups of the ligand side. The calculated binding energy of this latter configuration was −0.38 eV. Both binding energies were obtained by optimizing a snapshot of the configuration using DFT calculations. Then eventually, NH$_3$ further diffuses into a position in between four methyl groups each originating from different MTCP backbones as shown in panel (iii) of Fig. 4b and Fig. S12 (ESI†). The NH$_3$ binding energy of this geometry is −0.37 eV, where NH$_3$ entrapment is favored by the environment provided by the surrounding methyl groups. The calculated NH$_3$ binding energies of three main binding sites are summarized in Fig. 4c. Our DFT calculations showed that ammonium ion-like components (NH$_3$···H) and NH$_3$–Cu(I) can form in the presence of NH$_3$, which agrees well with our *in situ* DRIFT measurements. In overall, these calculations show that MTCPs have sufficient binding sites that can facilitate the efficient and strong adsorption of NH$_3$ molecules.

Doping effect on gas sensing properties

In an effort to further enhance the sensitivity toward NH$_3$, silver atoms were introduced into MTCP to create an Ag-doped structure (referring to Ag-MTCP). Silver-based composites are recognized for their high selectivity toward NH$_3$ gas.[50,51] Ag atoms were successfully introduced into MTCP through a simple stirring process at room temperature within just 2 hours, yielding Ag-doped MTCP. The amount of Ag in the materials is 0.1–0.3 at% overall. As shown in Fig. 5a, Ag-MTCP persevered its original nanowire morphology. EDS mapping was conducted to analyse the composition of Ag-MTCP, revealing a uniform distribution of each element (Cu, S, and Cl) along the NW.
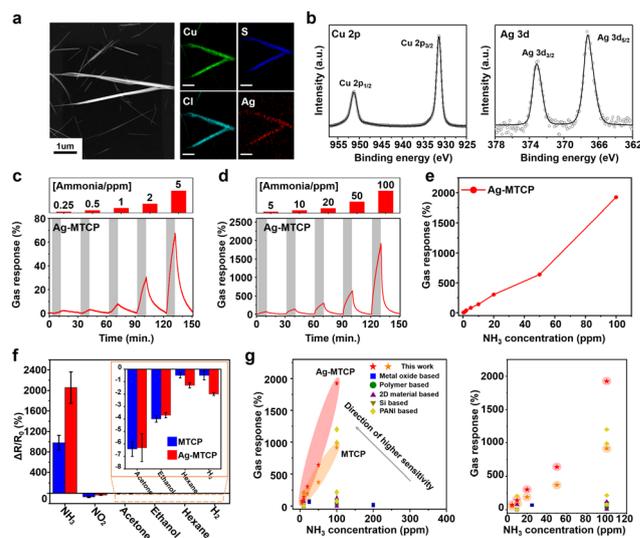

Fig. 5 (a) TEM image of overall morphology and EDS mapping result of Ag-MTCP (scale bar: 1 μm). (b) Cu 2p and Ag 3d XPS spectra of Ag-MTCP. (c) and (d) Dynamic gas response of Ag-MTCP towards (c) 0.25–5 ppm NH$_3$, (d) and 5–100 ppm NH$_3$. (e) Correlation between gas response of Ag-MTCP and NH$_3$ concentration. (f) Average gas response of MTCP and Ag-MTCP toward various gases. (g) Comparison of MTCP and Ag-MTCP with state-of-the-art sensors to detect NH$_3$ at room temperature. The graph on the right magnifies the region at low NH$_3$ concentrations.

Notably, Ag also exhibited a uniform distribution along the NW, with no significant accumulation in any particular region. Furthermore, the FTIR spectra and XRD patterns of Ag-MTCP were found to be consistent with those of the original MTCP (Fig. S13a and b, ESI†), indicating that the doping process did not induce any discernible change in the functional groups or chemical bonds. Fig. 5b showed the XPS spectra of Ag-MTCP. In Cu 2p XPS, the Cu 2p$_{3/2}$ peak at 931.38 eV suggests that Cu retained its +1 ionic state even after doping process. Moreover, in the Ag 3d spectrum, the Ag 3d$_{5/2}$ peak at 367.28 eV corresponds to Ag$^+$.[52] This observation indicated that Ag-MTCP was produced without the formation of metallic Ag during the Ag doping process. The XPS spectra for other elements were also comparable to those of the original MTCP (Fig. S14, ESI†).

The dynamic gas sensing response of Ag-MTCP toward 0.25–100 ppm NH$_3$ is shown in Fig. 5c and d where the graphs based on actual resistance values is in Fig. S15 (ESI†). Indeed, Ag-MTCP showed a gas response of 1925% for 100 ppm NH$_3$, which is twice higher than that of MTCP. Here, the Ag-MTCP sensor exhibited a response time of 378 s and a recovery time of 215 s toward 100 ppm NH$_3$ at room temperature. Fig. 5e compares the maximal gas response of Ag-MTCP toward 0.25–100 ppm NH$_3$, clearly showing the linear correlation similar to what was observed for MTCP. Furthermore, the gas response of Ag-MTCP under humid environments was also investigated, as shown in Fig. S16 (ESI†). While the gas response of Ag-MTCP toward 20 ppm NH$_3$ in a dry environment was 300%, the gas response was decreased to 160% in a 40% RH environment. A similar phenomenon was observed in MTCP where the gas response in a dry environment was

190%, decreasing to 120% in a 40% RH environment. This is expected to be due to partial screening of adsorption sites by water molecules.

We estimate that two factors contribute to the enhanced sensitivity after Ag doping. First, in a previous study, a polaron-hopping based conduction mechanism was proposed for this type of molecule where the transformation between Cu^+ and Cu^{2+} plays a major role.[53] While the redox behavior between Cu^+ and Cu^{2+} is known to be relatively reversible, Ag ions strongly prefer to exist as Ag^+ compared to Ag^{2+}, based on reduction potentials. Such a behavior can obstruct the hopping-based conduction mechanism, in which a large decrease in electrical conductivity was observed after Ag doping, as measured with the assistance of focused ion beam (FIB) analysis. (Fig. S17 and S18, ESI†). Second, Ag ions are also well known to bind with NH_3 to form ammine complexes, which can provide a synergistic effect.

In addition, MTCP and Ag-MTCP was tested against gases with various types of chemical moieties to investigate their gas sensing selectivity where the average gas response of multiple samples toward acetone, ethanol, hexane, H_2, and NO_2 was measured (Fig. 5f). Remarkably, this sensor exhibited a significant gas response, primarily to NH_3, with the exception of NO_2, although the respond is marginal. For example, the gas response of MTCP toward 100 ppm acetone and ethanol was -6.4% and -4.0%, respectively, which is a negligible value compared to the gas response toward NH_3 gas. These results show that MTCP-based sensors have a superior selectivity toward NH_3. Furthermore, the positive gas response toward NH_3 and negative gas response toward NO_2 suggests a p-type semiconductor-like behavior, which is in correspondence with the revealed electronic structure in Fig. 2d. Fig. 5g and Table S2 (ESI†) shows the state-of-the-art comparison of the gas sensing performance of various nanomaterials toward NH_3 under room temperature including metal oxides, polymers, and 2D materials. Detailed comparisons are shown in Table S2 (ESI†). It can be clearly seen that MTCP and Ag-MTCP is among the most sensitive NH_3 gas sensors to the best of our knowledge with a maximal gas response of 915% and 1925%, respectively, where previous reports show gas responses lower than 300% for 100 ppm NH_3. These results highlight the exceptional gas response of MTCPs at room temperature.

Conclusion

In conclusion, we develop a novel NH_3 gas sensor based on semiconducting, 1D-nanowire MTCPs, which exhibit remarkable gas response and selectivity at room temperature. Through the systematic analysis of X-ray crystallography and X-ray spectroscopy, we have unveiled the structural composition of MTCP, showing a 1D chain featuring Cu(ɪ) centers bonded to S atoms in MT ligand and Cl atoms. Furthermore, the molecular-level NH_3 reaction mechanism within the MTCP reveals that their outstanding NH_3 sensing capabilities results from the highly exothermic formation of NH_3–Cu and NH_3–H_3C complex, which were computationally predicted. Additionally, the doping of Ag atoms into MTCP has further enhanced both selectivity and reactivity of gas sensors, demonstrating a gas response of 1925%, which is one of the highest gas responses reported at room temperature. This research paves the way for the development of low-power, highly selective, and highly responsive gas sensing devices, with the potential to be used in multiple fields across the industry.

Author contributions

Taehun Im: conceptualization, data curation, formal analysis, investigation, writing – original draft, Juyun Lee: conceptualization, data curation, formal analysis, investigation, writing – original draft, Sung-Chul Kim: data curation, formal analysis, validation, Joharimanitra Randrianandraina: investigation, Joo-Won Lee: investigation, Myoung Won Chung: formal analysis, investigation, Taesung Park: formal analysis, investigation, Kam-Hung Low: investigation, Seungkyu Lee: investigation, Soong Ju Oh: resources, Yun Chan Kang: resources, Seunghyun Weon: resources, Jung-Hoon Lee: investigation, resources, Seon Joon Kim: conceptualization, funding acquisition, project administration, resources, supervision, writing – review & editing, Sohee Jeong: conceptualization, funding acquisition, project administration, resources, supervision, writing – review & editing.

Data availability

The data supporting this article have been included as part of the ESI.†

Conflicts of interest

There are no conflicts to declare.

Acknowledgements

References

1 D. Kwak, Y. Lei and R. Maric, *Talanta*, 2019, **204**, 713–730.

2 Z. S. Hosseini, A. I. zad and A. Mortezaali, *Sens. Actuators, B*, 2015, **207**, 865–871.

3 J. Zhang, X. Liu, G. Neri and N. Pinna, *Adv. Mater.*, 2016, **28**, 795–831.

4 X. Duan, Z. Duan, Y. Zhang, B. Liu, X. Li, Q. Zhao, Z. Yuan, Y. Jiang and H. Tai, *Sens. Actuators, B*, 2022, **369**, 132302.

5 C. Liu, H. Tai, P. Zhang, Z. Yuan, X. Du, G. Xie and Y. Jiang, *Sens. Actuators, B*, 2018, **261**, 587–597.

6 S. Wang, Y. Jiang, B. Liu, Z. Duan, H. Pan, Z. Yuan, G. Xie, J. Wang, Z. Fang and H. Tai, *Sens. Actuators, B*, 2021, **343**, 130069.

7 Y. Zhang, J. Zhang, Y. Jiang, Z. Duan, B. Liu, Q. Zhao, S. Wang, Z. Yuan and H. Tai, *Sens. Actuators, B*, 2020, **319**, 128293.

8 J. Xiong, Y. Cai, X. Nie, Y. Wang, H. Song, H. M. A. Sharif, Z. Li and C. Li, *Sens. Actuators, B*, 2023, **390**, 133987.

9 X. Liu, W. Zheng, R. Kumar, M. Kumar and J. Zhang, *Coord. Chem. Rev.*, 2022, **462**, 214517.

10 J. Lopez-Molino and P. Amo-Ochoa, *ChemPlusChem*, 2020, **85**, 1564–1579.

11 S. M. Majhi, A. Ali, P. Rai, Y. E. Greish, A. Alzamly, S. G. Surya, N. Qamhieh and S. T. Mahmoud, *Nanoscale Adv.*, 2022, **4**, 697–732.

12 L. E. Kreno, K. Leong, O. K. Farha, M. Allendorf, R. P. Van Duyne and J. T. Hupp, *Chem. Rev.*, 2012, **112**, 1105–1125.

13 B. J. Holliday and T. M. Swager, *Chem. Commun.*, 2005, 23–36.

14 X. Deng, J. Y. Hu, J. Luo, W. M. Liao and J. He, *Top. Curr. Chem.*, 2020, **378**, 27.

15 M. Aust, A. J. Herold, L. Niederegger, C. Schneider, D. C. Mayer, M. Drees, J. Warnan, A. Pothig and R. A. Fischer, *Inorg. Chem.*, 2021, **60**, 19242–19252.

16 L. Sun, M. G. Campbell and M. Dinca, *Angew. Chem., Int. Ed.*, 2016, **55**, 3566–3579.

17 L. Sun, T. Miyakai, S. Seki and M. Dinca, *J. Am. Chem. Soc.*, 2013, **135**, 8185–8188.

18 A. A. Sagade and R. Sharma, *Sens. Actuators, B*, 2008, **133**, 135–143.

19 T. Fu, *Sens. Actuators, B*, 2015, **212**, 487–494.

20 Y. Zhang, P. Xu, J. Xu, H. Li and W. Ma, *J. Phys. Chem. C*, 2011, **115**, 2014–2019.

21 M. Bendahan, C. Jacolin, P. Lauque, J.-L. Seguin and P. Knauth, *J. Phys. Chem. B*, 2001, **105**, 8327–8333.

22 B. Wolpert, M. Leitl, A. Pfitzner and V. M. Mirsky, *Sens. Actuators, B*, 2008, **134**, 839–842.

23 J. Conesa-Egea, F. Zamora and P. Amo-Ochoa, *Coord. Chem. Rev.*, 2019, **381**, 65–78.

24 G.-N. Liu, X.-N. Tang, J.-S. Guo, Q.-S. Liu, C. Ye, C. Li, G. Xu and G.-E. Wang, *Sens. Actuators, B*, 2024, **399**, 134864.

25 D. Lee, S. J. Lee, J. H. Kim, J. Park, Y. C. Kang, M. Song, H. W. Lee, H. S. Kim and J. W. Choi, *Adv. Funct. Mater.*, 2022, **32**, 2202207.

26 M. S. Kim, H. Park, S. O. Won, A. Sharma, J. Kong, H. S. Park, Y. M. Sung, T. J. Park, M. W. Moon and K. Hur, *Small*, 2019, **15**, e1903197.

27 G. S. Pawley, *J. Appl. Crystallogr.*, 1981, **14**, 357–361.

28 A. A. Coelho, *J. Appl. Crystallogr.*, 2018, **51**, 210–218.

29 G. M. S. El-Bahy, B. A. El-Sayed and A. A. Shabana, *Vib. Spectrosc.*, 2003, **31**, 101–107.

30 H. S. Adhikari, A. Garai, K. D. Manandhar and P. N. Yadav, *ACS Omega*, 2022, **7**, 30978–30988.

31 M. A. Raza, K. Javaid, U. Farwa, A. Javaid, M. Yaseen, J. K. Maurin, A. Budzianowski, B. Iqbal and S. Ibrahim, *J. Mol. Struct.*, 2023, **1271**, 133989.

32 J. Li, J. Huang, Y. Zhang, Y. Wang, C. Xue, G. Jiang, W. Liu and C. Zhu, *RSC Adv.*, 2016, **6**, 58786–58795.

33 L. Jin, L. Cai, D. Chen, W. Wang, H. Shen and F. Zhang, *J. Mater. Sci.*, 2019, **54**, 12650–12658.

34 M. C. Biesinger, B. R. Hart, R. Polack, B. A. Kobe and R. S. C. Smart, *Miner. Eng.*, 2007, **20**, 152–162.

35 A. Mohtasebi, A. D. Broomfield, T. Chowdhury, P. R. Selvaganapathy and P. Kruse, *ACS Appl. Mater. Interfaces*, 2017, **9**, 20748–20761.

36 K. Henzler, A. Heilemann, J. Kneer, P. Guttmann, H. Jia, E. Bartsch, Y. Lu and S. Palzer, *Sci. Rep.*, 2015, **5**, 17729.

37 K. O. Kvashnina, S. M. Butorin, A. Modin, I. Soroka, M. Marcellini, J. H. Guo, L. Werme and J. Nordgren, *J. Phys.: Condens. Matter*, 2007, **19**, 226002.

38 M. A. Rizvi, S. A. Akhoon, S. R. Maqsood and G. M. Peerzada, *J. Anal. Chem.*, 2015, **70**, 633–638.

39 A. M. Elseman, *Sci. Rep.*, 2023, **13**, 7939.

40 R. K. Hocking, E. C. Wasinger, F. M. F. de Groot, K. O. Hodgson, B. Hedman and E. I. Solomon, *J. Am. Chem. Soc.*, 2006, **128**, 10442–10451.

41 S. B. Harkins, N. P. Mankad, A. J. M. Miller, R. K. Szilagyi and J. C. Peters, *J. Am. Chem. Soc.*, 2008, **130**, 3478–3485.

42 P. Aslanidis, P. J. Cox, S. Divanidis and A. C. Tsipis, *Inorg. Chem.*, 2002, **41**, 6875–6886.

43 G. M. Su, H. Wang, B. R. Barnett, J. R. Long, D. Prendergast and W. S. Drisdell, *Chem. Sci.*, 2020, **12**, 2156–2164.

44 B. R. Barnett, H. A. Evans, G. M. Su, H. Z. H. Jiang, R. Chakraborty, D. Banyeretse, T. J. Hartman, M. B. Martinez, B. A. Trump, J. D. Tarver, M. N. Dods, L. M. Funke, J. Borgel, J. A. Reimer, W. S. Drisdell, K. E. Hurst, T. Gennett, S. A. FitzGerald, C. M. Brown, M. Head-Gordon and J. R. Long, *J. Am. Chem. Soc.*, 2021, **143**, 14884–14894.

45 W. Zhou, Y. Liu, Y. Yang and P. Wu, *J. Phys. Chem. C*, 2014, **118**, 6448–6453.

46 F. Giordanino, E. Borfecchia, K. A. Lomachenko, A. Lazzarini, G. Agostini, E. Gallo, A. V. Soldatov, P. Beato, S. Bordiga and C. Lamberti, *J. Phys. Chem. Lett.*, 2014, **5**, 1552–1559.

47 K. Kang, X. Yao, Y. Huang, J. Cao, J. Rong, W. Zhao, W. Luo and Y. Chen, *J. Hazard. Mater.*, 2021, **416**, 125821.

48 J. Liu, X. Li, Q. Zhao, J. Ke, H. Xiao, X. Lv, S. Liu, M. Tadé and S. Wang, *Appl. Catal., B*, 2017, **200**, 297–308.

49 R. Millan, P. Cnudde, A. E. J. Hoffman, C. W. Lopes, P. Concepcion, V. van Speybroeck and M. Boronat, *J. Phys. Chem. Lett.*, 2020, **11**, 10060–10066.

50 S. Cui, H. Pu, G. Lu, Z. Wen, E. C. Mattson, C. Hirschmugl, M. Gajdardziska-Josifovska, M. Weinert and J. Chen, *ACS Appl. Mater. Interfaces*, 2012, **4**, 4898–4904.

51 F. Wei, Y. Zhong, H. Luo, Y. Wu, J. Fu, Q. He, J. Cheng, J. Na, Y. Yamauchi and S. Liu, *J. Mater. Chem. A*, 2021, **9**, 8308–8316.

52 W. Shao, Y. R. Chen, F. Xie, H. Zhang, H. T. Wang and N. Chang, *RSC Adv.*, 2020, **10**, 38174–38183.

53 B. L. Suh, G. Kang, S. M. Yoon, S. Cho, M. W. Moon, Y. M. Sung, M. S. Kim and K. Hur, *Adv. Mater.*, 2023, **35**, e2206980.